Research in Astron. Astrophys. **2013** Vol. **13** No. **3**, 359–372
http://www.raa-journal.org *http://www.iop.org/journals/raa*

Research in Astronomy and Astrophysics

Data processing and error analysis for the CE-1 Lunar microwave radiometer *

Jian-Qing Feng, Yan Su, Jian-Jun Liu, Yong-Liao Zou and Chun-Lai Li

National Astronomical Observatories, Chinese Academy of Sciences, Beijing 100012, China; *suyan@nao.cas.cn*

Received 2011 December 18; accepted 2012 August 20

Abstract The microwave radiometer (MRM) onboard the Chang' E-1 (CE-1) lunar orbiter is a 4-frequency microwave radiometer, and it is mainly used to obtain the brightness temperature ($T_{\rm B}$) of the lunar surface, from which the thickness, temperature, dielectric constant and other related properties of the lunar regolith can be derived. The working mode of the CE-1 MRM, the ground calibration (including the official calibration coefficients), as well as the acquisition and processing of the raw data are introduced. Our data analysis shows that $T_{\rm B}$ increases with increasing frequency, decreases towards the lunar poles and is significantly affected by solar illumination. Our analysis also reveals that the main uncertainty in $T_{\rm B}$ comes from ground calibration.

Key words: space vehicles — instruments: microwave radiometer — Moon: brightness temperature — method: data processing — error analysis

1 INTRODUCTION

Passive microwave remote sensing of the Moon began in the 1940s. The thermal radio emission of the Moon was first detected at the 1.25 cm wavelength by Dicke & Beringer (1946). Subsequently, Piddington & Minnett (1949) performed a series of observations at the same wavelength over three lunar cycles. In their comprehensive series of observations of the Moon, it was pointed out that the variation of the Moon's brightness temperature ($T_{\rm B}$) was roughly sinusoidal with an amplitude considerably lower than what was observed for the infrared emission. With the construction of large radio telescopes in subsequent decades, more and more researchers have paid attention to radio observations of the Moon.

As one of the main payloads on the Chang' E-1 (CE-1) orbiter, the microwave radiometer (MRM) is used to obtain the distribution of $T_{\rm B}$ on the lunar surface. This is the first attempt in human history to measure the brightness of the lunar surface with the aid of a space-borne passive microwave radiometer. The MRM is a full-power microwave radiometer and its working frequencies include 3.0, 7.8, 19.35 and 37 GHz. Its view is only in the nadir direction with the observing instrument facing the lunar surface. Figure 1 is the installation diagram of the CE-1 MRM.

* Supported by the National Natural Science Foundation of China.

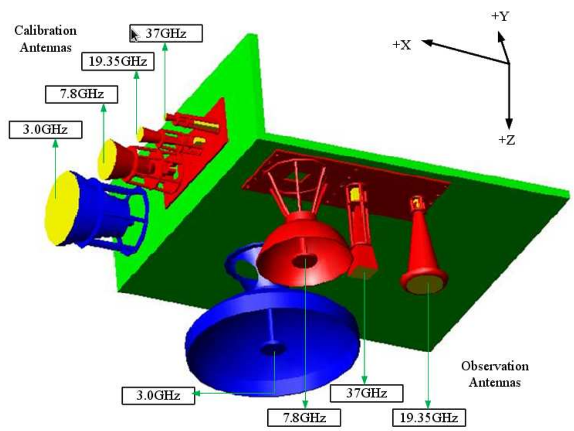

Fig. 1 Installation Diagram of the MRM on CE-1: four observation antennas are equipped along the $+Z$ axis of the satellite's body coordinate system, pointing in the direction of the lunar surface; four cold space calibration antennas are installed along the $+X$ axis, which is the orbiting direction for the satellite. The X, Y and Z axes of the satellite's body coordinate system correspond respectively to the roll, pitch and yaw axes.

2 DATA FEATURES

For each frequency of the MRM, there are three different input sources: the observation antenna viewing the lunar surface, the calibration antenna for measuring cold space, and the hot matched load. The three inputs share one receiver, so the MRM works in a two-point calibration mode. The real-time temperature matched load is used as the high temperature calibration source, and the cosmic microwave background (CMB) provides the low temperature calibration source. We use the high and low temperature sources to calculate the $T_{\rm B}$ obtained by the observing antenna through a calibration equation. Furthermore, equipped with a temperature measurement circuit, the physical temperature of 28 key points in the MRM can be measured by attached platinum resistance sensors. The temperature data will be included into the transmitted scientific data so that they can provide a reference for calibration correction. Details about onboard instruments and ground calibrations were described by Wang et al. (2010).

During the whole detection period of the MRM, there is no large variation in the internal temperature of the instruments, so the working state is stable.

From Figure 2, we find that the working temperature of the receivers for all orbits where detections occur are between 285 K$\sim$298 K. The temperature variations of each orbital period are no more than 5 K, which satisfies the requirement of normal operation of the instrument.

MRM observation antennas are fixed on the +Z axis, and the field of view is related to the detection frequency, meaning that the radius of the main beam footprint on the Moon for the 3.0 GHz channel is 50 km, but the corresponding radius of the main beam footprint for 7.8, 19.35 and 37 GHz is 35 km. Every observation of the MRM represents the total microwave radiation of the lunar surface in the region of the footprint. Figure 3 displays the scope of the footprints on the lunar surface and their corresponding center points.

The CE-1 orbiter moves along a polar orbit (orbital inclination is greater than 88°) and it takes the obiter about 128 min to complete a cycle around the Moon. When working in orbit, the four MRM receivers periodically receive calibration and observing signals, and the signal recording period is 11.6 s. During one period, it takes 0.8 s to input signals from the calibration antenna, followed

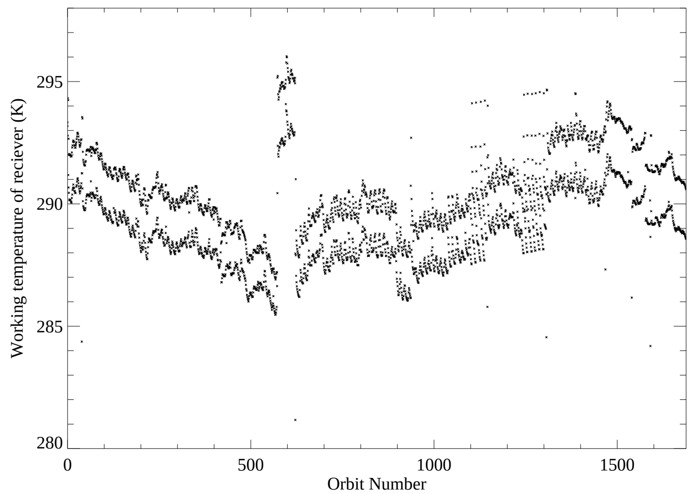

Fig. 2 Temperature variations of the MRM receivers during the entire detection period. In each orbital detection period we choose the highest and the lowest temperatures. Upper points stand for the highest temperature and lower points for the lowest. The horizontal axis shows the detection orbit number, and the vertical axis indicates the receiver temperature.

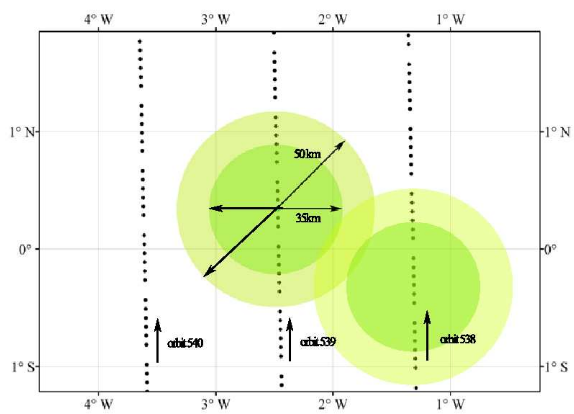

Fig. 3 The scope of footprints for the main beam on the lunar surface and the center points of the footprints for four channels. Black points represent the centers of the footprints, green circles represent the footprint regions of 7.8, 19.35 and 37 GHz, and yellow is for 3.0 GHz. This figure shows the distribution of the footprint centers of three neighboring orbits (538, 539, 540) on the lunar surface near the equatorial region, while the orbiter is moving from south to north.

by another 0.8 s to input signals from the heat load, then 9.6 s to input signals from the observation antenna, and the remaining 0.4 s is the standby time. The signal sampling integration time is 40 ms, so the data acquisition period in each channel will generate multiple observing signals and calibration signals. After the receiver receives different signals, they will be converted to corresponding voltage output and then expressed as binary data.

While operating normally, there are six observational data generated during a signal recording period for each channel, and the data interval is 1.6 s. The MRM records almost 4000 detection data in total during an orbit. Each datum represents the average value of the T_B within the footprint. Along the flight direction (latitude), the distance between centers of adjacent footprints is about 2.27 km, so the degree of overlap for footprints is high. However, along the horizontal direction (longitude), the degree of overlap for footprints is related to the track pitch, and the track pitch in the equatorial region is about 35 km. In the region near the lunar equator, the footprints of two adjacent tracks, taken with high frequency, are collinear. The overlap of footprints, taken with low frequency along parallel tracks, cover 18.8% of the area. The higher the latitude that the satellite moves, the smaller the track pitch is, and the higher the degree of overlap becomes for parallel footprints.

3 DATA ACQUISITION AND COVERAGE

The CE-1 MRM started working at 23:23 on 2007 November 27, and stopped working at 19:11 on 2009 January 14. During this period, the total operating time for MRM was 3984.4 hours, during which the available recording time for data was 3363.1 hours (about 1690 orbits). The data acquisition rate was over 84.4% and the accumulated observational data cover the whole lunar surface. During the flight phase, the MRM operation time can be divided into four periods, and statistics of the data for each time period are shown in Table 1.

Table 1 CE-1 MRM Scientific Data Acquisition Sheet

No	CE-1 flight control period	Working time (h)	Available data recording time (h)	Data acquisition rate (%)
1	2007.11.27∼2008.01.27	1380.7	1160.3	84
2	2008.01.30∼2008.02.04	120.9	100.4	83
3	2008.05.15∼2008.07.29	1624.6	1396.6	86
4	2008.11.12∼2009.01.14	858.2	705.8	82
	Total	3984.4	3363.1	84.4

In addition, during the early stage of satellite operation, the satellite's orbit was about 200 km high, while in the extension period, the satellite's orbital altitude was reduced to about 100 km. Thus, after 2008 December 10, the remaining 210 tracks of data were obtained at an orbital altitude of about 100 km.

The time period required for CE-1 to return to a given footprint area is about one month. During the intervening time, MRM tracks are evenly distributed over the entire lunar surface, which we call "coverage." There are two types of coverages within a month: one is under the condition of illumination (lunar day), the other is under the condition of non-illumination (lunar night). However, due to instrument failure or shadow, some areas on the lunar surface may not have been covered during a given track of data acquisition. Those areas that were missed would then be covered during the next return to the track.

Figure 4 shows the number of times different parts of the lunar surface were covered with MRM data in a homolographic grid (each grid block in the equatorial region is $2^\circ \times 2^\circ$, about 3678 km^2) during the whole phase of data acquisition. During the lunar day, regions in the lunar nearside, defined by W70°∼E40°, and farside, defined by E160°∼W130°, are covered by MRM footprints more frequently than the areas in the region W20°∼W60°. The maximum number of repeated cycles for a given spot is nine. The situation of coverage at lunar night is symmetric with that in lunar day. The minimum number of cycles on the lunar surface is one. There are no areas that are not covered by footprints.

4 DATA PROCESSING

CE-1 detection data were received and processed by using the Ground Research and Application System (GRAS) affiliated with the National Astronomical Observatories, Chinese Academy of

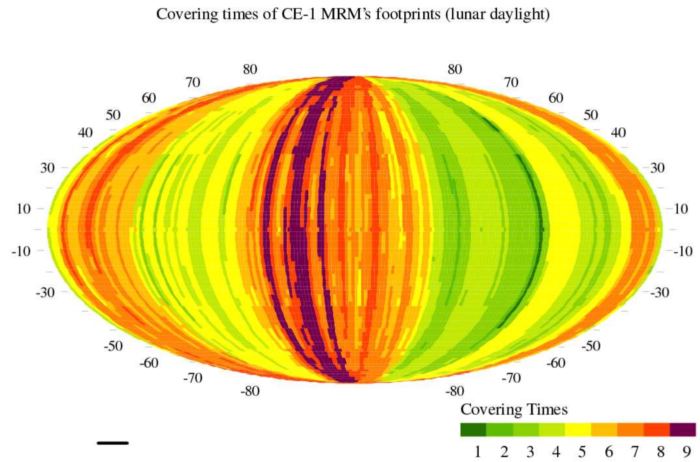

Fig. 4 The number of times areas on the lunar surface are covered by MRM data in lunar daylight during the CE-1 data acquisition phase. In this figure, the lunar surface is divided into 11 306 homolographic grid blocks, and the colors in the grid system represent the number of times a given region is covered by observations. This figure adopts the Mollweide projection, also called a homolographic projection, where the coordinate system is the lunar body-fixed reference system. The coverage at lunar night is symmetric with that in lunar day.

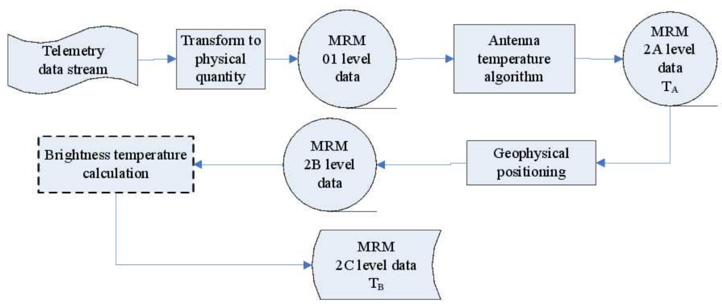

Fig. 5 MRM data processing flow. From 01 data to the final released 2C data, the MRM data processing can be divided into three stages: antenna temperature algorithms, geometric positioning, and brightness temperature calculation, corresponding to three levels of data. 01 data – MRM original voltage data; 2A data – MRM antenna temperature data; 2B data – MRM geometric positioning data; 2C data – lunar surface T_{B} data; T_{A} – observation antenna temperature; T_{B} – brightness temperature on the lunar surface.

Sciences (NAOC). Through conversion of physical quantities, satellite bit stream data were transformed from binary data to ASCII files. These data represent the original voltage value of each observation of the radiometer that we call raw data. After being processed by an antenna temperature algorithm, as well as performing geometric positioning and T_{B} calculations, the raw data were converted into T_{B} on the lunar surface for each observation. Figure 5 shows the MRM data processing flow.

According to the MRM working mode, there are seven records in a period, and each recording interval is 1.6 s. The first record represents calibration data, including five voltage outputs of cold sky and five voltage outputs of a hot load within 1.6 s in each channel. The second to seventh records are observational data, each containing 40 voltage outputs from each channel. The calibration data are used for the calibration of observational data.

The antenna temperature algorithm is the first stage of the MRM data processing flow. During this process, the input is 01 level voltage data and the output is antenna temperature at the 2A level. This algorithm includes the following steps: a) elimination of invalid data; b) averaging of the calibration data; c) averaging of the observation data; d) calibration of the antenna temperature $T_{\rm A}$. The first step is to check the validity of the data, and remove invalid data points (mainly referred to as over-range data and padding data). The average of calibration data is the arithmetic mean of five calibration output voltages of each channel within 1.6 s. The average of observational data is the arithmetic mean of 40 output voltages of each channel within 1.6 s. After computing the running average, the antenna temperature is calculated by using the average observed voltage, calibration voltage and hardware radiative transfer model. Section 5 of this paper will discuss the specific process of antenna temperature calibration.

Geometric positioning uses the satellite's attitude, orbital information and ephemeris to solve the latitude and longitude of the footprint's center corresponding to the MRM $T_{\rm B}$ data, as well as solar altitude and azimuth. The data level is 2B.

For the calculation of brightness temperature, the conversion between antenna temperature $T_{\rm A}$ and $T_{\rm B}$ on the lunar surface is (Ulaby et al. 1981)

$$T_A = \frac{\iint\limits_{4\pi} T_{\rm B}(\theta,\phi) F_{\rm n}(\theta,\phi) d\Omega}{\iint\limits_{4\pi} F_{\rm n}(\theta,\phi) d\Omega}. \tag{1}$$

Here $d\Omega$ is the solid angle differential, $F_{\rm n}(\theta,\phi)$ is the antenna pattern, θ is the pitch angle and ϕ is the azimuth angle. This is a convolution relationship. In order to get the precise distribution of $T_{\rm B}$, we need sufficiently dense data on the lunar surface to perform the deconvolution. In the data processing of the CE-1 MRM, we directly treat antenna temperature $T_{\rm A}$ as the distribution of $T_{\rm B}$ without deconvolution.

5 GROUND CALIBRATION TEST

5.1 Hardware Radiative Transfer Model and Calibration Equations

The model used for the signal flow from three different input sources to the receiver of each channel is shown in Figure 6.

$T_{\rm A}$ represents the total microwave radiation that the antenna receives. $\alpha_{\rm w}$ and $\alpha_{\rm s}$ are the power transmission coefficients through the waveguide, switch and isolator. $T_{\rm w}$ and $T_{\rm s}$ are the physical temperatures of these components. $\Gamma_{\rm wl}$ and $\Gamma_{\rm wr}$ are the power reflection coefficients of the reflection plane between the antenna and the waveguide when viewing from left and right respectively, and $\Gamma_{\rm sl}$ and $\Gamma_{\rm sr}$ are the power reflection coefficients of the reflection plane between the waveguide and the switching isolator when viewing from left and right respectively. For the calibration of a signal from cold space, the corresponding physical quantities are: $T_{\rm c}$, $\alpha_{\rm w-c}$, $\alpha_{\rm s-c}$, $T_{\rm w-c}$, $T_{\rm s-c}$, $\Gamma_{\rm wl-c}$, $\Gamma_{\rm wr-c}$, $\Gamma_{\rm sl-c}$ and $\Gamma_{\rm sr-c}$; for the calibration of a signal from a hot load, the equivalent brightness temperature of the load is $T_{\rm h}$.

$T_{\rm A}{}'$ stands for the effective antenna temperature at the output port of the switch and isolator mounted on the front, as shown in Figure 6, which can be given by (Wang et al. 2010)

$$T_{\rm A}{}' = T_{\rm A}(1-\Gamma_{\rm wl})\alpha_{\rm w}(1-\Gamma_{\rm sl})\alpha_s$$

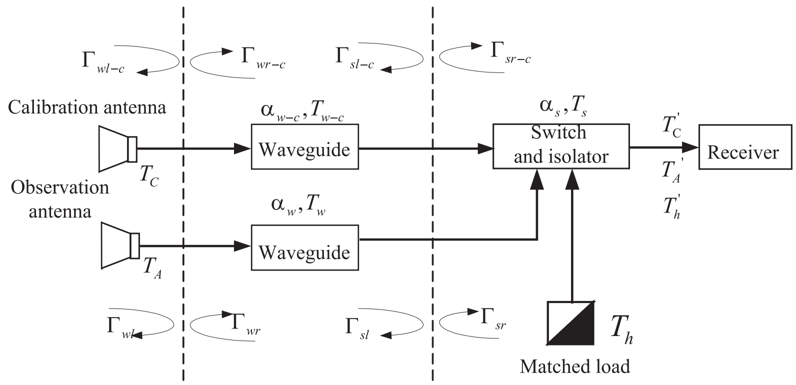

Fig. 6 Hardware radiative transfer model for the MRM (Wang et al. 2010).

$$+T_{\rm w}(1-\alpha_{\rm w})(1-\Gamma_{\rm sl})\alpha_s(1+\alpha_{\rm w}\Gamma_{\rm wr})$$
$$+T_{\rm s}[(1-\alpha_s)+\alpha_s|\Gamma_{\rm sr}{}^{1/2}+(1-\Gamma_{\rm sl})^{1/2}(1-\Gamma_{\rm sr})^{1/2}\Gamma_{\rm wr}{}^{1/2}\alpha_{\rm w}e^{j2\theta_A}|^2] \quad (2)$$

where $\theta_A = \frac{2\pi}{\lambda} l_A$ is the electric phase of the two reference planes in the data flow for an observation, and l_A is the length of the waveguide. The model of the calibration of a signal from cold space is the same as that for the data flow for an observation and the resulting equation is similar to that derived above, which can be given by (Wang et al. 2010)

$$\begin{aligned} T_{\rm c}' = \ & T_{\rm c}(1-\Gamma_{\rm wl-c})\alpha_{\rm w-c}(1-\Gamma_{\rm sl-c})\alpha_{\rm s-c} \\ & +T_{\rm w-c}(1-\alpha_{\rm w-c})(1-\Gamma_{\rm sl-c})\alpha_{\rm s-c}(1+\alpha_{\rm w-c}\Gamma_{\rm wr-c}) \\ & +T_{\rm s-c}[(1-\alpha_{\rm s-c})+\alpha_{\rm s-c}|\Gamma_{\rm sr-c}{}^{1/2} \\ & +(1-\Gamma_{\rm sl-c})^{1/2}(1-\Gamma_{\rm sr-c})^{1/2}\Gamma_{\rm wr-c}{}^{1/2}\alpha_{\rm w-c}e^{j2\theta_c}|^2], \end{aligned} \quad (3)$$

where $T_{\rm c}'$ is the total thermal emission leaving the output port of the switch and isolator, $T_{\rm c}$ is the cold-space temperature, and its value depends on the temperature value received by the calibration antenna. Without contamination, the value of $T_{\rm c}$ is generally 2.7 K, equivalent to the temperature from CMB radiation. If some radiative objects enter into the view of the calibration antenna, we need to establish a model to calculate the real $T_{\rm c}$. For the signal from a hot load, since the load is directly connected to the switch and their physical temperatures are approximately equal, the thermal emission at the receiver is

$$T_{\rm h}' = T_{\rm h} = T_{\rm s} = T_{\rm s-c}. \quad (4)$$

Let $V_{\rm A}$, $V_{\rm H}$ and $V_{\rm C}$ denote the average output voltage of the signal from an observation, hot load and cold space through the receiver, respectively. According to the two-point calibration principle, the effective antenna temperature of the observation can also be given by (Wang et al. 2010)

$$T_{\rm A}' = \frac{V_{\rm A}-V_{\rm C}}{V_{\rm H}-V_{\rm C}}T_{\rm h}' + \frac{V_{\rm H}-V_{\rm A}}{V_{\rm H}-V_{\rm C}}T_{\rm c}'. \quad (5)$$

By substituting Equations (2), (3) and (4) into Equation (5), we can obtain the observation antenna temperature $T_{\rm A}$ described by

$$T_{\rm A} = \left[\frac{V_{\rm A}-V_{\rm C}}{V_{\rm H}-V_{\rm C}}T_{\rm h} + \frac{V_{\rm H}-V_{\rm A}}{V_{\rm H}-V_{\rm C}}(c_1T_{\rm c}+c_2T_{\rm w-c}+c_3T_{\rm h}) - a_2T_{\rm w} - a_3T_{\rm h}\right]/a_1, \quad (6)$$

where

$$
\begin{aligned}
a_1 &= (1-\Gamma_{\rm wl})\alpha_{\rm w}(1-\Gamma_{\rm sl})\alpha_s,\\
a_2 &= (1-\alpha_{\rm w})(1-\Gamma_{\rm sl})\alpha_s(1+\alpha_{\rm w}\Gamma_{\rm wr}),\\
a_3 &= [(1-\alpha_s)+\alpha_s|\Gamma_{\rm sr}{}^{1/2}+(1-\Gamma_{\rm sl})^{1/2}(1-\Gamma_{\rm sr})^{1/2}\Gamma_{\rm wr}{}^{1/2}\alpha_{\rm w}e^{j2\theta_A}|^2],\\
c_1 &= (1-\Gamma_{\rm wl-c})\alpha_{\rm w-c}(1-\Gamma_{\rm sl-c})\alpha_{\rm s-c},\\
c_2 &= (1-\alpha_{\rm w-c})(1-\Gamma_{\rm sl-c})\alpha_{\rm s-c}(1+\alpha_{\rm w-c}\Gamma_{\rm wr-c}),\\
c_3 &= [(1-\alpha_{\rm s-c})+\alpha_{\rm s-c}|\Gamma_{\rm sr-c}{}^{1/2}+(1-\Gamma_{\rm sl-c})^{1/2}(1-\Gamma_{\rm sr-c})^{1/2}\Gamma_{\rm wr-c}{}^{1/2}\alpha_{\rm w-c}e^{j2\theta_{\rm c}}|^2].
\end{aligned}
\tag{7}
$$

Equation (6) is the calibration equation of $T_{\rm A}$, where physical temperatures $T_{\rm w-c}$, $T_{\rm w}$ and $T_{\rm h}$ can be obtained by platinum resistance sensors, while the calibration coefficients a_1, a_2, a_3, c_1, c_2 and c_3 are determined by the ground calibration test before launch.

5.2 Ground Calibration Test and Calibration Coefficients

From Equation (6), it can be shown that the accuracy of calibration coefficients significantly affects the temperature value derived from the observation antenna. Thus, the environment used for ground calibration should be close to the environment of space for the satellite during its orbit.

The calibration test is operated by the MRM developer, which is the Center for Space Science and Applied Research, Chinese Academy of Sciences (CSSAR, CAS) (Wang et al. 2010). Due to the limitations of the experimental conditions, the ground test was not operated in a vacuum environment but at room temperature and ambient pressure, which means it is not a conventional thermal vacuum (T/V) test (Njoku et al. 1980; Ruf et al. 1995). The test was divided into three parts. The first part was normal observation, where the antenna observes a variable temperature source, and the cold-space antenna observes a cold blackbody. The variable temperature source was adjusted over the range of 100 K$\sim$320 K. In the second part, the cold-space antenna was covered by a piece of absorbing foam at normal temperature. In the third part, the cold-space antenna observed the variable temperature source at high temperature (320 K) and intermediate temperature (190 K or 220 K), while the observation antenna was viewing absorbing material or microwave anechoic chamber walls. After obtaining calibration data, calibration coefficients were determined by a set of linear equations.

Table 2 lists the current calibration coefficients used in antenna temperature calibration, and these coefficients were officially provided by the MRM developer, CSSAR.

Table 2 MRM Calibration Coefficients Used in Antenna Temperature Calibration (officially provided by CSSAR)

Channel	c_1	c_2	c_3	a_1	a_2	a_3
3.0 GHz	0.694257	0.006533	0.294746	0.635737	0.078466	0.304281
7.8 GHz	0.502442	0.111982	0.382320	0.554733	0.069104	0.372222
19.35 GHz	0.600903	0.040674	0.363698	0.621588	0.067002	0.311620
37 GHz	0.367357	0.075114	0.557492	0.451888	0.061286	0.488930

In the ground calibration tests, the radiometer was always exposed to the air and the tests were carried out at a normal temperature, which is not representative of a space environment. Consequently, there must be some errors if the calibration coefficients are directly applied to the processing of the observational data taken in orbit.

6 RESULTS OF DATA PROCESSING AND ERROR ANALYSIS

6.1 Results of Data Processing

Through data processing, we obtain the values of $T_{\rm B}$ on the lunar surface, then we can make the distribution map of the entire lunar surface by using the accumulated data. Figure 7 shows maps of

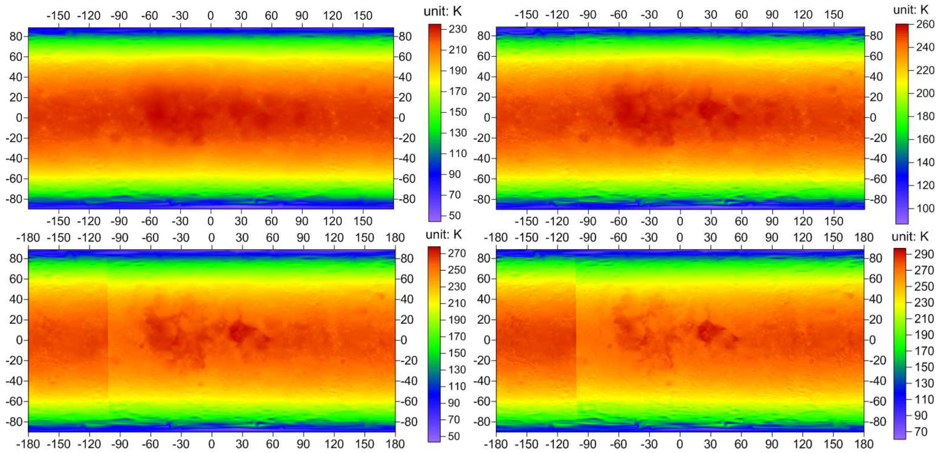

Fig. 7 Interpolated maps of the T_{B} distribution on the lunar surface obtained by the MRM in the first month of detection during the lunar day. Upper left is 3 GHz, upper right is 7.8 GHz, lower left is 19.35 GHz, and lower right is 37 GHz. The maps use a simple cylindrical projection and Kriging interpolation method. Interpolation involves 520 000 data points, and the spatial resolution is 18.2 km. The transverse "discontinuity" in the map results from the conjunction of the first track and the last track within one month; their T_{B} values are different because the solar incidence angle is quite different.

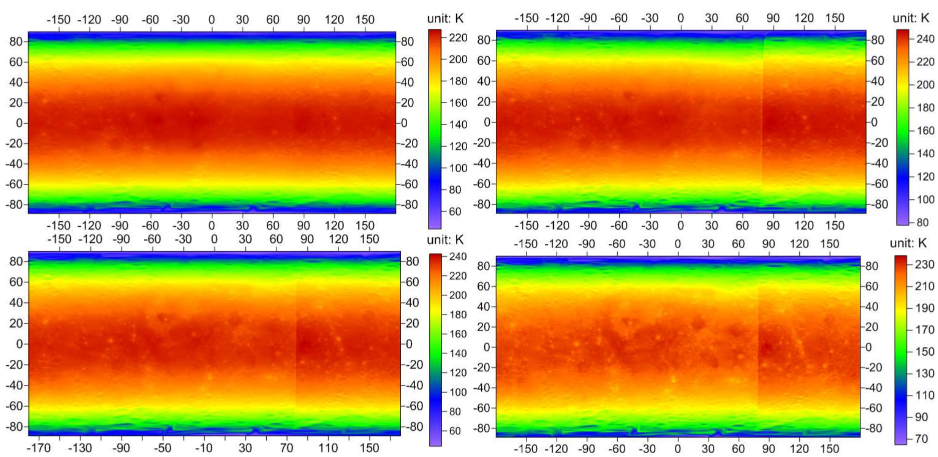

Fig. 8 Interpolated maps of the T_{B} distribution on the lunar surface obtained by the MRM in the first month of detection during the lunar night. Upper left is 3 GHz, upper right is 7.8 GHz, lower left is 19.35 GHz, and lower right is 37 GHz. The maps use a simple cylindrical projection and Kriging interpolation method. Interpolation involves 520 000 data points, and the spatial resolution is 18.2 km. The cause of the transverse "discontinuity" in the maps is the same as that in Figure 7.

the distribution of T_{B} over the lunar surface during lunar daylight, using data obtained by the MRM in the first month. Figure 8 shows the corresponding maps of T_{B} over the lunar surface at lunar night. The data processing results of the first month of detection show that:

(a) During lunar daylight, the range of T_{B} for 3 GHz on the lunar surface is 37.4 K$\sim$235.4 K; the range of 7.8 GHz is 88.0 K$\sim$260.4 K; the range of 19.35 GHz is 47.1 K$\sim$278.3 K; the range of 37 GHz is 65.3 K$\sim$297.2 K. At lunar night, on the lunar surface the range of $T_{\rm B}$ for 3 GHz is 49.5 K$\sim$227.6 K; the range of 7.8 GHz is 81.1 K$\sim$248.3 K; the range of 19.35 GHz is 46.3 K$\sim$232.8 K; the range of 37 GHz is 64.6 K$\sim$238.6 K.

(b) The $T_{\rm B}$ for four channels during lunar daylight in the same areas have the relationship that is 37 GHz $>$ 19.35 GHz $>$ 7.8 GHz $>$ 3.0 GHz, and the $T_{\rm B}$ at lunar night in the same areas is lower than the $T_{\rm B}$ during lunar day for the same channel. As seen from the angle of the entire distribution, the data processing results are similar to the recent observation from a ground-based radio telescope (Morabito et al. 2008; Zhang et al. 2012): The trend of the distribution is that the $T_{\rm B}$ is higher in areas with low latitude but lower in polar areas.

(c) Checking the $T_{\rm B}$ distribution map on the lunar surface (especially during the daylight), we can find topographic information about the lunar surface. In the 37.0 GHz $T_{\rm B}$ map, even the impact craters on the Moon can be distinguished, especially in lunar polar areas. One of the main factors affecting the $T_{\rm B}$ on the lunar surface is the physical temperature, and this physical temperature is constrained by topography. So the $T_{\rm B}$ in some areas on the lunar surface is also affected by topography.

(d) Through comparison of the map of the distribution of $T_{\rm B}$ and the geological map of the lunar surface, it can be found that, during the lunar daylight the $T_{\rm B}$ is higher in the mare on the near side of the Moon. This is because the mare surface consists primarily of basalt, while anorthosite rock is distributed in the highlands. Basalt is generally made of silicate minerals with a high content of iron and titanium, and it has the property of high dielectric loss and shallow penetration depth of microwave radiation, so the $T_{\rm B}$ of the mare is relatively high. By contrast anorthosite is made of silicate minerals with a high content of magnesium, aluminum and calcium, and it has properties of low dielectric loss and deep penetration depth of microwave radiation, so the $T_{\rm B}$ for the highland is relatively low.

6.2 Error Analysis

According to the antenna calibration Equation (6) and error propagation formula, the error from the antenna temperature calibration equation $\Delta T_{\rm A}$ can be expressed with functions of the RMS error of each term representing variation in the equation

$$\begin{aligned}\Delta T_{\rm A}^2 = \Delta T^2 + \Delta V^2 &\left[\left(\frac{\partial T_{\rm A}}{\partial V_{\rm A}}\right)^2 + \left(\frac{\partial T_{\rm A}}{\partial V_{\rm H}}\right)^2 + \left(\frac{\partial T_{\rm A}}{\partial V_{\rm C}}\right)^2\right] \\ &+ \Delta T_n^2 \left[\left(\frac{\partial T_{\rm A}}{\partial T_{\rm h}}\right)^2 + \left(\frac{\partial T_{\rm A}}{\partial T_{\rm w}}\right)^2 + \left(\frac{\partial T_{\rm A}}{\partial T_{\rm w-c}}\right)^2\right] \\ &+ \Delta T_{\rm c}^2 \left(\frac{\partial T_{\rm A}}{\partial T_{\rm c}}\right)^2. \end{aligned} \tag{8}$$

In the equation:

(1) ΔT represents the sensitivity of the receiver, approximately 0.5 K.
(2) ΔV is the quantization error of the voltage value, ΔV = 0.1525 mV.
(3) ΔT_n is the measurement error of the platinum resistance sensors. With no record of error analysis from sensors on the CE-1 MRM sensors in the ground calibration test report, we refer to the CE-2 MRM ground calibration results provided by CSSAR and define $\Delta T_n \leqslant$ 0.08 K.
(4) $\Delta T_{\rm c}$ is the uncertainty in the temperature of cold space. In Equation (6), we simply treat the CMB radiation value of 2.7 K as the temperature of cold space. But when CE-1 takes data over high latitude areas ($\geqslant$70°) of the Moon, the Sun and Earth may enter into the view of the cold-space antenna, leading to contamination. According to the calculation results of Cui et al.

(2009), taking contamination into account, variation of $T_{\rm c}$ could reach 10 K, which means $\Delta T_{\rm c} \leqslant 10$ K.

Thus, putting all the error terms above into our calculation, we will find that in the absence of cold-space contamination, the calibration error of antenna temperature is mainly affected by the sensitivity of the receiver, and $\Delta T_{\rm A} \leqslant 0.5$ K. If there is cold-space contamination when data are obtained over the high latitude area of the Moon, $\Delta T_{\rm A} \leqslant 7.6$ K.

If taking nonlinearity (Mo 1996) of the receiver into consideration, Equation (5) needs to be amended. A nonlinear term Q should be added to Equation (5), the expression of which is given as

$$Q = \mu \left[\frac{T_{\rm h}{}' - T_{\rm c}{}'}{V_{\rm H} - V_{\rm C}} \right]^2 (V_{\rm A} - V_{\rm H})(V_{\rm A} - V_{\rm C}), \tag{9}$$

where μ is a nonlinear coefficient, and its value is influenced by the working temperature of the instruments.

As Table 2 does not contain nonlinear coefficient μ, in the data processing methodology, the final calculation of $T_{\rm A}$ does not actually contain nonlinear terms, which means $Q = 0$. This will lead to a nonlinearity in error ΔT_Q (the CE-2 MRM ground calibration results indicate that under the condition of working temperature 298 K, ΔT_Q of each channel is: 3.0 GHz channel -3 K$\leqslant \Delta T_Q \leqslant$5; 7.8 GHz channel –0.5 K$\leqslant \Delta T_Q \leqslant$9 K; 19.35 GHz channel –3.5 K$\leqslant \Delta T_Q \leqslant$3 K; and 37 GHz channel –1.5 K$\leqslant \Delta T_Q \leqslant$4 K).

In the stage of calculating the brightness temperature, observation antenna temperature $T_{\rm A}$ is treated like the value $T_{\rm B}$ on the lunar surface; in other words, $T_{\rm B} = T_{\rm A}$. Therefore, the final error of $T_{\rm B}$ on the lunar surface should also include the antenna's sidelobe contribution, temperature transmission loss from the lunar surface to the antenna, and the radiation loss caused by antenna efficiency (these three errors are small and could be combined into ΔT_a).

In summary, the total error of $T_{\rm B}$ can be expressed by

$$\Delta T_{\rm B} = \sqrt{\Delta T_{\rm A}^2 + \Delta T_Q^2 + \Delta T_a^2}. \tag{10}$$

The error of $T_{\rm B}$ in low-latitude areas is smaller than that in high-latitude areas. This is because the error in a low-latitude area is mainly from the nonlinearity, but error sources in a high-latitude area include nonlinearity and contamination from cold space. Since the ground calibration test report does not give the nonlinear coefficient μ and ΔT_a, it is unable to accurately calculate the error of $T_{\rm B}$ obtained by the CE-1 MRM, but we estimate that the value of $\Delta T_{\rm B}$ could be no more than 10 K.

Different from the MRM, various sources of ground truth, including ground-based microwave radiometers, radiosondes, global climatological models, Amazon rain forest models and ocean models, can be used for validation and in-flight calibration of the radiometers onboard Earth orbiters (Ruf et al. 1994). Due to the lack of a standard reference on the Moon, it is difficult to evaluate the MRM data, so we can make a comparison between Earth-based observation and MRM data. In the 10 cm range, Koshchenko et al. (1962) observed the Moon using a 22 m radio telescope, and they found the average value of the Moon's brightness temperature at λ=9.6 cm was 230$\pm$4.5 K, with little variation in terms of lunar phase. Another measurement made by Medd & Broten (1961) showed that the brightness temperature at the lunar equator using 3.2 GHz was 220 K, and no variation with lunar phase was detected. In 2004, Morabito et al. (2008) observed the Moon by using the NASA DSS 34 m antenna at 2.3 GHz (S-band), 8.4 GHz (X-band) and 32 GHz (Ka-band), and the maximum brightness temperatures at these frequencies were 230 K, 258 K and 280 K on the lunar equator. For another frequency, Zelinskaya et al. (1959) gave an expression of the temperature of radio emissions from the central portion of the lunar disk at a wavelength of 1.63 cm, as a function of lunar phase: $T_{\rm c} = 224 - 36 \cos$ (Ωt–40), where the phase of the new Moon corresponds to $\Omega t = 0$. The brightness temperatures obtained by the CE-1 MRM at 3.0 GHz and 7.8 GHz approximately coincide with

Earth-based radio observations, but the results at 19.35 GHz and 37 GHz are higher than those by about 10 K. Because of the low resolution of Earth-based observations, these comparisons are not completely accurate.

The analysis above is based on the assumption that there are no problems with the calibration coefficients. Actually, due to the inadequate calibration before launch, there could be some systematic errors which may be greater than the errors listed above. The same problems exist in some other radiometer explorations with similar instrument structures, such as the Mariner 2 Microwave Radiometer experiment on Venus (at the wavelength of 19 mm, the estimated error is 5%, whereas the results for 13.5 mm have an error of 25%; Barath et al. 1964) and the Earth observing mission Seasat Scanning Multichannel Microwave Radiometer (which has large-scale systematic errors (Milman & Wilheit 1985)). In Section 7, we will discuss the influence from the calibration coefficients.

7 EXISTING PROBLEMS AND DISCUSSIONS

The CE-1 MRM has obtained a large amount of scientific data. Data processing includes an algorithm for computing antenna temperature, as well as geometric positioning and brightness temperature calculations. The final $T_{\rm B}$ of the lunar surface is the observation antenna temperature.

Regarding the error that arises from deriving $T_{\rm B}$, several relevant error sources are listed in Section 6. The contamination from cold space can be calculated by establishing a physical model and the sidelobe contribution can also be eliminated through deconvolution. Progress in this area will be made by updating the data processing model in the future. Error in the ground calibration coefficient, which is related to the test environment, test method and test data processing method, has the greatest influence on the final results for $T_{\rm B}$ (Njoku et al. 1980; Ruf et al. 1995). Processing ground calibration test data is complex and important work, and different methods will lead to different coefficient values.

Table 3 shows another set of ground calibration coefficients and nonlinear coefficients proposed by CSSAR (Wang et al. 2010).

We compare the $T_{\rm B}$ calculation result processed with two sets of calibration coefficients in Tables 2 and 3. Figures 9 and 10 show the difference of the single-track observation result and the difference for the entire lunar surface result, respectively.

From Figure 10, it can be found that different calibration coefficients have little effect on the distribution trend of $T_{\rm B}$ over the entire lunar surface, but they actually generate greater deviations for the exact value of $T_{\rm B}$. Generally, the minimum difference exists on the lunar equator, and the maximum difference exists at the lunar poles. For the channel of 3.0 GHz, the difference is the biggest among the four channels. The average difference on the equator is -9.3 K, while at the lunar poles it is -27.8 K, and the difference range for the full Moon is -43.3 K$\sim$ -7.3 K. The percentage of difference for polar regions reaches 20%$\sim$30% (assuming that $T_{\rm B}$ in the polar regions is 100 K). In the channel of 7.8 GHz, the difference is the smallest. They are both about 7 K at the equator and lunar poles, and the range for the difference over the full Moon is -1.8 K$\sim$ 14.9 K. The differences of data results are shown in Table 4.

Table 3 Ground Calibration Coefficients and Nonlinear Coefficients Proposed by Wang et al. (2010)

Channel	c_1	c_2	c_3	a_1	a_2	a_3	μ
3.0 GHz	0.448413	0.042766	0.515045	0.503422	0.019832	0.484782	0.000722
7.8 GHz	0.392663	0	0.587391	0.455423	0	0.548911	0.000667
19.35 GHz	0.425253	0	0.577018	0.55624	0.309955	0.165837	0.000793
37 GHz	0.356748	0	0.644538	0.477458	0.039196	0.4875	0.000524

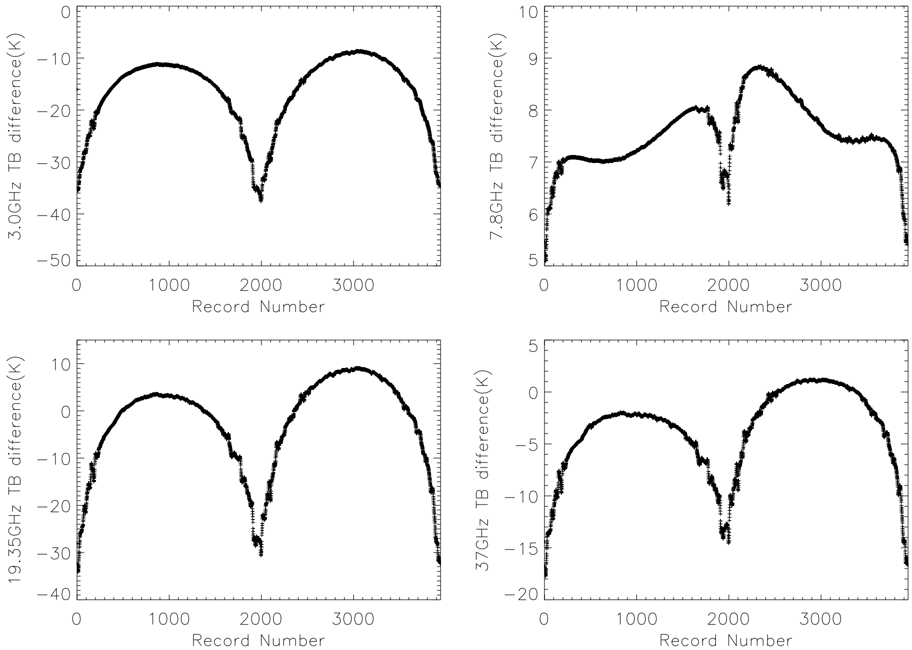

Fig. 9 The difference of $T_{\rm B}$ calculated from Table 2 coefficients and Table 3 coefficients (within the 445th detection orbit). Abscissa is the number of records, and the ordinate is the difference of $T_{\rm B}$ (unit: K). Upper left is 3 GHz, upper right is 7.8 GHz, lower left is 19.35 GHz and lower right is 37 GHz.

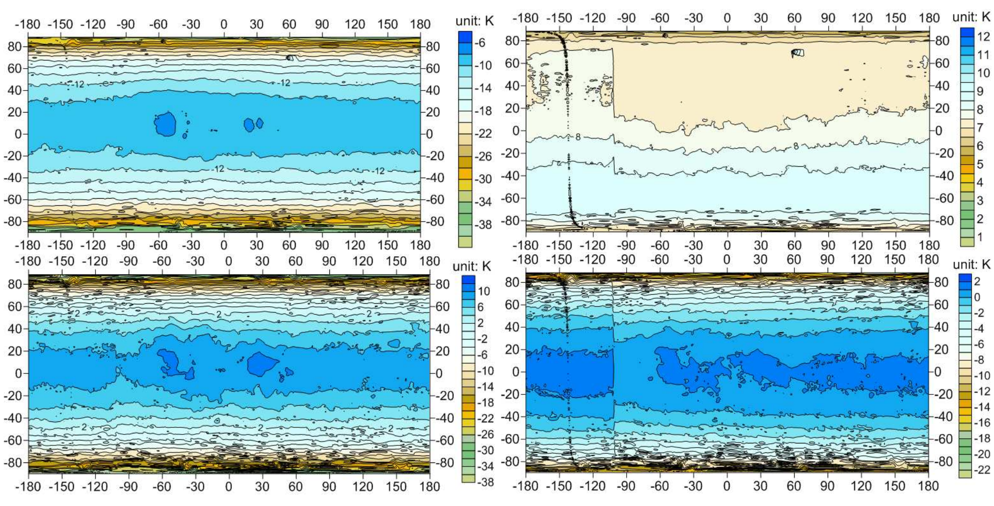

Fig. 10 The difference of $T_{\rm B}$ calculated from Table 2 coefficients and Table 3 coefficients in lunar daylight. Upper left is 3 GHz, upper right is 7.8 GHz, lower left is 19.35 GHz and lower right is 37 GHz. The maps use a simple cylindrical projection, and the Kriging interpolation method. The spatial resolution is 18.2 km.

Table 4 Difference of T_B Result Calculated with Coefficients of Tables 2 and 3 (unit: K)

Frequency	Statistic	Polar region ($70° \sim 90°$)	Mid-latitude ($30° \sim 70°$)	Equator ($0° \sim 30°$)	Entire Moon
3.0 GHz	Mean difference	-27.8	-14.4	-9.3	-15.7
	Standard error	5.2	3.2	0.9	7.6
	Difference range	$-43.3 \sim -7.3$	$-8.7 \sim -24.6$	$-12.1 \sim -7.5$	$-43.3 \sim -7.3$
7.8 GHz	Mean difference	7.3	8.0	7.8	7.8
	Standard error	0.8	0.7	0.4	0.7
	Difference range	$-1.8 \sim 14.9$	$2.8 \sim 11.7$	$6.8 \sim 9.7$	$-1.8 \sim 14.9$
19.35 GHz	Mean difference	-17.2	1.6	8.2	-0.3
	Standard error	7.6	3.9	1.0	10.4
	Difference range	$-37.1 \sim -3.6$	$-12.3 \sim 9.2$	$5.1 \sim 11.7$	$-37.1 \sim 11.7$
37 GHz	Mean difference	-9.0	-1.5	0.9	-2.3
	Standard error	3.4	1.4	0.3	4.1
	Difference range	$-24.7 \sim 1.7$	$-8.2 \sim 2.6$	$-0.8 \sim 2.0$	$-24.7 \sim 2.6$

Though there is a great difference between the result calculated with coefficients from Table 2 and that using Table 3, the T_B data published by GRAS at present are still calculated with the calibration coefficients in Table 2, which are officially provided by the developer of MRM (CSSAR).

Acknowledgements This work is supported by the National Natural Science Foundation of China (Grant No. 11173038). We thank CSSAR for providing the calibration coefficient of MRM. We acknowledge the referee for his suggestions on our manuscript.

References

Barath, F. T., Barrett, A. H., Copeland, J., Jones, D. E., & Lilley, A. E. 1964, AJ, 69, 49
Cui, H. Y., Wang, Z. Z., Zhang, X. H., & Dong, X. L. 2009, Remote Sensing Technology and Application, 24, 435
Dicke, R. H., & Beringer, R. 1946, ApJ, 103, 375
Koshchenko, V. N., Kuzmin, A. D., & Salomonovich, A. E. 1962, in IAU Symposium, 14, The Moon, eds. Z. Kopal, & Z. K. Mikhailov, 497
Medd, W. J., & Broten, N. W. 1961, Planet. Space Sci., 5, 307
Milman, A. S., & Wilheit, T. T. 1985, J. Geophys. Res., 90, 11631
Mo, T. 1996, IEEE Transactions on Microwave Theory Techniques, 44, 1460
Morabito, D. D., Imbriale, W., & Keihm, S. 2008, IEEE Transactions on Antennas and Propagation, 56, 650
Njoku, E. G., Stacey, J. M., & Barath, F. T. 1980, IEEE Journal of Oceanic Engineering, 5, 100
Piddington, J. H., & Minnett, H. C. 1949, Australian Journal of Chemistry, 2, 63
Ruf, C. S., Keihm, S. J., & Janssen, M. A. 1995, IEEE Transactions on Geoscience and Remote Sensing, 33, 125
Ruf, C. S., Keihm, S. J., Subramanya, B., & Janssen, M. A. 1994, J. Geophys. Res., 99, 24915
Ulaby, F. T., Moore, R. K., & Fung, A. K. 1981, Microwave Remote Sensing: Active and Passive, 1 (Addison-Wesley Pub. Co., Advanced Book Program/World Science Division)
Wang, Z., Li, Y., Zhang, X., et al. 2010, Science China Earth Sciences, 53, 1392
Zelinskaya, M. R., Troitskii, V. S., & Fedoseev, L. I. 1959, Soviet Ast., 3, 628
Zhang, X.-Z., Gray, A., Su, Y., et al. 2012, RAA (Research in Astronomy and Astrophysics), 12, 1297